

Spatially deconvolved optical coherence tomography

Peter D. Woolliams,¹ Robert A. Ferguson,¹ Christian Hart,¹
Alex Grimwood,² and Peter H. Tomlins^{1,*}

¹Biophotonics Group, National Physical Laboratory, Hampton Road, Middlesex TW11 0LW, UK

²Royal Institution of Great Britain, 21 Albemarle Street, London W1S 4BS, UK

*Corresponding author: pete.tomlins@npl.co.uk

Received 18 November 2009; revised 2 March 2010; accepted 11 March 2010;
posted 12 March 2010 (Doc. ID 120141); published 1 April 2010

In this paper we present spatially mapped point-spread function (PSF) measurements of an optical coherence tomography (OCT) instrument and subsequent spatial deconvolution. The OCT B-scan image plane was divided into 2400 subimages, for which PSFs were determined from OCT measurements of a specially designed phantom. Each PSF was deconvolved from its corresponding subimage of the phantom using the Lucy–Richardson algorithm. Following deconvolution, all of the subimages were reassembled to form a final deconvolved image, from which the resolution improvement was quantitatively assessed. The lateral resolution was found to improve by $3.1\ \mu\text{m}$ compared to an axial resolution enhancement of $4.5\ \mu\text{m}$. The spatial uniformity of both axial and lateral resolution was also observed to increase following deconvolution, demonstrating the advantage of deconvolving local PSFs from their associated subimages. © 2010 Optical Society of America

OCIS codes: 110.4500, 100.1830, 330.6130, 350.5730, 350.4800.

1. Introduction

Novel optical imaging technology is increasingly important in both medical [1] and industrial [2] applications. One technique that is receiving much attention in these fields, for noninvasive two- and three-dimensional (2D and 3D) imaging, is optical coherence tomography (OCT) [3]. OCT has attractive attributes, offering resolution in the region of $2\text{--}20\ \mu\text{m}$, both laterally and axially [4,5], with the ability to image to depths of several mm, depending on the sample opacity [6,7] and instrument sensitivity. Acquisition speeds are also favorable, with real-time acquisition of 3D data sets now possible over a scale of several mm [8]. A feature unique to OCT is that the axial and lateral resolutions are decoupled, each being governed by separate optical phenomena. In the axial dimension, it is the coherence length of the optical source, and in the lateral dimension, it

is diffraction that imposes physical resolution limits. Resolution can be considered to be arbitrarily defined from the system impulse response, or point-spread function (PSF), that would be observed upon measurement of an infinitesimally small object. Knowledge of the PSF of an instrument facilitates and, hence, improved resolution. Furthermore, PSF deconvolution may facilitate traceability for objective and quantitative tissue pathology assessment, making measurements intercomparable.

Ralston *et al.* have previously developed a numerical method for Gaussian beam waist compensation in OCT, known as interferometric synthetic aperture microscopy [9,10]. Microspheres embedded in a silicone matrix were used to image the PSF and qualitatively verify performance of the technique. Wang [11] and Schmitt [12] have applied axial PSF deconvolution methods to improve depth resolution in OCT. Liu *et al.* have considered both lateral and axial PSF to perform a 2D deconvolution in OCT [13]. However, in their work, a 2D PSF was estimated from the source coherence function and Gaussian

beam optics, yielding a single point approximation to the true PSF, ignoring the variation in PSF as a function of both depth and lateral position. In this article we use epoxy resin phantoms doped with a low density of iron oxide particles to estimate the 2D PSF at multiple locations across the B-scan image plane of an OCT microscope. These spatially independent PSF measurements are deconvolved from their corresponding region of the OCT image, thus yielding a PSF corrected OCT B-scan. The aim of this work is twofold. First, we measured resolution parameters of an OCT instrument and spatially mapped them onto the B-scan image plane. Second, we deconvolved the measured instrument PSFs from OCT image data. We demonstrate the efficacy of this method by applying the correction to an OCT data set of the PSF phantom itself and comparing analysis before and after deconvolution.

2. Theory

A. Axial and Lateral Resolution

The axial and lateral resolutions of an OCT instrument are independently dominated by coherence and diffraction, respectively. By considering only the instrument optics, neglecting the effect of sample-induced aberrations, the OCT PSF can be approximated by a 2D Gaussian function $h(x, z)$:

$$h(x, z) = A \exp \left\{ - \left[\frac{(x - x_0)^2}{w_x^2} + \frac{(z - z_0)^2}{w_z^2} \right] \right\}, \quad (1)$$

where x and z represent the orthogonal transverse and axial directions, respectively. The e^{-1} radius along these axes are w_x and w_z , related to the full width at half-maximum (FWHM) by

$$\Delta x = 2w_x \sqrt{\ln 2}, \quad (2)$$

$$\Delta z = 2w_z \sqrt{\ln 2}. \quad (3)$$

A 2D Gaussian is a reasonable approximation of the PSF under the assumption of a light source with a Gaussian spectral intensity distribution and an approximately Gaussian sample beam profile, as expected from a single-mode optical fiber launch typically used in OCT light sources. Physically, the axial resolution Δz is defined in terms of the source coherence function as [3,14]

$$\Delta z = 0.44 \frac{\lambda_0^2}{\Delta \lambda}. \quad (4)$$

The source spectral FWHM is given by $\Delta \lambda$, and λ_0 is the source center wavelength. Equation (4) does not account for the sample refractive index n that causes Δz to scale as n^{-1} . While Eq. (4) is derived on the basis of a Gaussian spectral intensity distribution, it is a reasonable approximation for other smooth, symmetrical frequency domain filters, such as the Hann,

Hamming, and Blackman windows. However, if the source spectral shape becomes highly asymmetric or structured, then the validity of Eq. (4) becomes questionable [15,16]. The approximately Gaussian mode obtained from a single-mode optical fiber launch system facilitates the use of Gaussian beam optics to describe propagation of the probe beam in space [17]. The field e^{-1} radius w_i of a focused, illuminating Gaussian beam varies along the optical axis z according to

$$w_i(z) = w_0 \sqrt{1 + \left(\frac{z - z_0}{z_R} \right)^2}, \quad (5)$$

reducing to w_0 at the focus ($z = z_0$). The Rayleigh range of the incident field $z_R = \pi w_0^2 \lambda_0^{-1}$. Under these conditions, in the absence of a sample, the corresponding FWHM beam waist is

$$\Delta x_i = 2w_0 \sqrt{\ln 2}. \quad (6)$$

However, due to mixing of the probe beam with the reference beam in the OCT interferometer, there is a $2^{-1/2}$ enhancement of the detected beam width that yields a detected field radius of [18]

$$w_x = \frac{w_0}{\sqrt{2}}. \quad (7)$$

The associated detected beam waist,

$$w_d(z) = w_x \sqrt{1 + \left(\frac{z - z_0}{z_R} \right)^2}, \quad (8)$$

yields a lateral resolution parameter of

$$\Delta x = 2w_x \sqrt{\frac{\ln 2}{2}} \approx 0.37 \frac{\lambda}{\text{NA}}, \quad (9)$$

where NA is the numerical aperture of the focusing lens. As light propagates from air into the higher refractive index sample, the numerical aperture is reduced ($\text{NA}_{\text{sample}} = \text{NA}/n$). However, the effect of diffraction is also reduced within the sample, owing to the change in optical wavelength within the sample, i.e., $\lambda_{\text{sample}} = \lambda/n$. Hence, in Eq. (7), the refractive index is canceled. Therefore, neglecting higher order aberrations, lateral resolution is independent of sample refractive index [19].

B. Point-Spread Function

The output of an imaging system $g(x, y)$ is described mathematically by a convolution of its PSF $h(x, y)$ with an input signal $f(x, y)$ that represents the object being imaged [20]:

$$g(x, y) = \int_{-\infty}^{\infty} f(x - x_0, y - y_0) h(x_0, y_0) dx_0 dy_0. \quad (10)$$

Hence, if the object is sufficiently small to approximate a delta function, i.e., $f(x, y) \approx \delta(x, y)$, then the

output of the imaging system is a measurement of its PSF. Therefore, measurement of a suspension of sub-resolution particles using OCT facilitates spatial mapping of the PSF.

3. Materials and Methods

A. Phantom Preparation

A solid PSF phantom was made from a two-part polyurethane resin (DR006, Atlas Polymers, UK), doped with a low density of red iron oxide spheroidal nanoparticles (07674, Polysciences, Incorporated, USA), having a predominant diameter of 400 nm, from a distribution spanning 300–800 nm. These particles are highly reflective in the near infrared, compared to previously used glass microspheres. In order to avoid speckle, the phantom was designed to have an average particle spacing L between 25 and 50 μm . To achieve this experimentally, the required mass–volume ratio of iron oxide particles (m) to polyurethane (V) was determined from $m/V = M/L^3$, where M is the mass of a single iron oxide particle and L is the target particle spacing. This equation is derived based on the assumption that the particle diameter is small compared to the spacing and that each particle occupies the center of a cube of edge length L . The mean particle spacing of approximately 30 μm was estimated by counting the number of particles in the focal volume of the 3D OCT data. The particles were distributed uniformly within the lower viscosity part of the resin by excitation in an ultrasonic bath. The two parts were mixed using an overhead stirrer for 5 min, ensuring sample homogeneity. The composite was poured into a 25 mm diameter cylindrical mold to a nominal depth of 15 mm and degassed at a pressure of 0.15 bar for 10 min and left to cure at 60 °C for 12 h. The phantom surface was polished to a flatness of a few visible wavelengths across the 25 mm diameter, verified using a Fizeau interferometer (Mk 2 Interferometer, Zygo Corporation, USA), and demonstrated by the typical result in Fig. 1. The surface form error was <75 nm peak to valley over a 2 mm scan, with a local roughness of <25 nm, measured using a white light surface profilometer (Coherence Correlation Interferometer, Taylor Hobson, UK); see Fig. 2.

The phantom surface was tilted at 5° from normal to the OCT probe beam, thereby avoiding the strong Fresnel backreflection from the sample surface.

B. Spatial Point-Spread Function Measurement

Images of the PSF phantom were obtained using a commercial swept source OCT microscope (EX1301, Michelson Diagnostics Limited, UK). Previous measurements of this instrument have given axial and lateral resolution parameters of $\Delta z = 10.9 \pm 0.2 \mu\text{m}$ and $\Delta x = 8.4 \pm 0.2 \mu\text{m}$, respectively. These are consistent with the center wavelength of 1310 nm and 75 nm bandwidth specified for the light source (HSL-2000, Santec, Japan) and objective numerical aperture of 0.059 ± 0.001 [21] measured using a

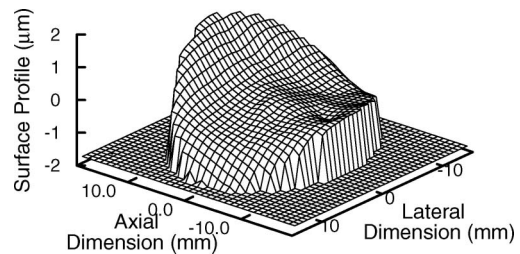


Fig. 1. Surface flatness over the total area of the 25 mm diameter phantoms.

beam profiler. In order to measure sufficient data points to gain insight into the statistical distribution of results, measurements of the phantom were obtained over a 3D volume. The volume comprised a series of B-scans, each 8 mm wide by 3 mm depth, with an A-scan spacing of 4.4 μm . The inter-B-scan spacing was 4 μm over an acquisition range of 1 mm. Two copies of the OCT data were used during processing, the “measurement” data were left as measured, from which located PSFs were obtained. The “localization” data set was processed such that individual points could be located in the “measurement” data. Initially the “localization” data were prepared as a series of sequential, depth resolved B-scans, scaled linearly in field amplitude. This was achieved in the usual manner for a spectral domain OCT system, i.e., the spectral interference pattern corresponding to each A-scan was divided by a reference spectrum, resampled from linear wavelength to linear frequency space, multiplied by a Hann window function, and fast Fourier transformed (FFT) into the spatial domain. The linear field amplitude A-scan was obtained from the magnitude of the FFT. A key component of the point extraction is background subtraction, which removes persistent image artifacts and interface signals from the data set, leaving only the data points of interest. An estimate of the background signal was obtained by taking a rolling mean of 20 adjacent B-scans relative to each B-scan. It was assumed that the background signal was slowly varying compared to the individual points signal. The estimated background signal was subtracted from each B-scan, leaving only the data points of interest. Following background subtraction,

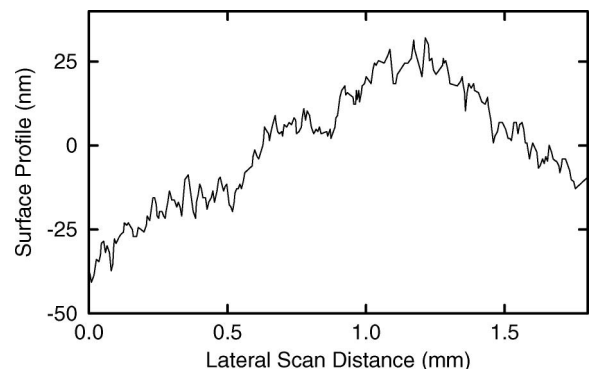


Fig. 2. Typical phantom surface profile indicating local surface height variations of less than 100 nm.

a binary image of each B-scan was formed by setting all points greater than 40% of maximum field amplitude to 1 and all else to 0. The binary image served as a PSF location map, enabling identification of PSFs in the unaltered “measurement” data. A 21×21 pixel data area was extracted around each located PSF in the “measurement” data set. Equation (1) was fitted to each extracted PSF to obtain estimates of Δx and Δz by minimizing the sum of the square residuals R^2 between the measured and the fitted data, $h_{\text{meas}}(x, z)$ and $h(x, z)$, respectively, over all N measurements within the extracted PSF:

$$R^2 = \frac{1}{N} \sum_{n=1}^N [h_{\text{meas}}(x_n, z_n) - h(x_n, z_n)]^2. \quad (11)$$

Several steps were taken to ensure that only single points contributed to the analysis. The fitted values for Δx and Δz were required to be smaller than the width of the point grid. Additionally, the center of each fitted point was also required to be located within the 21×21 pixel area with a nonnegative amplitude. These constraints, plus the monitoring of the sum of the squared residuals, resulted in a conservative point acceptance rule and led to approximately 250 points per B-scan being identified and contributing to the final results. The B-scan image space was divided into an 80×30 grid of $100 \times 100 \mu\text{m}$ subimages, onto which each resolution parameter was mapped, averaging those that were spatially coincident. It was found to be advantageous to weight the averages based upon the reciprocal of R^2 , hence reducing contributions to the final result from relatively poor fits, such as those that occur when multiple high intensity points are detected within

a single 21×21 pixel area. In this way, spatial maps of the axial and lateral resolution were formed. Each of the measured PSFs were approximated by a 2D Gaussian function, according to the resolution parameters determined for the corresponding subimage. The Gaussian PSFs were deconvolved from their corresponding OCT subimages in each B-scan. Subimages in which no PSF fit was obtained were approximated by an average 2D Gaussian, for which Δx and Δz were the mean of all fitted values. Deconvolution was carried out on OCT data scaled linearly in intensity. 2D deconvolution in each subimage was accomplished using the Lucy–Richardson algorithm, previously investigated for OCT by Liu *et al.* This algorithm is described in detail elsewhere in the literature [22]. The implementation applied here was from the MATLAB Imaging Processing Toolbox, using 10 iterations with a damping parameter of three times the linear OCT data standard deviation to suppress noise generation. The set of deconvolved B-scans were reprocessed as described above to estimate the improvement in PSF and its spatial uniformity.

4. Results

Resolution parameters for approximately 25×10^3 PSFs were determined, spatially distributed throughout the acquired data volume. Identified points from a single B-scan are marked in Fig. 3(a) by a square centered around the highest intensity pixel. Each square represents a subimage to which the 2D Gaussian fit was applied. An example single PSF measurement is shown in Fig. 3(b). Axial and lateral cross sections of the PSF in Figs. 3(c) and 3(d) demonstrate that the instrument PSF is well approximated by the 2D Gaussian function.

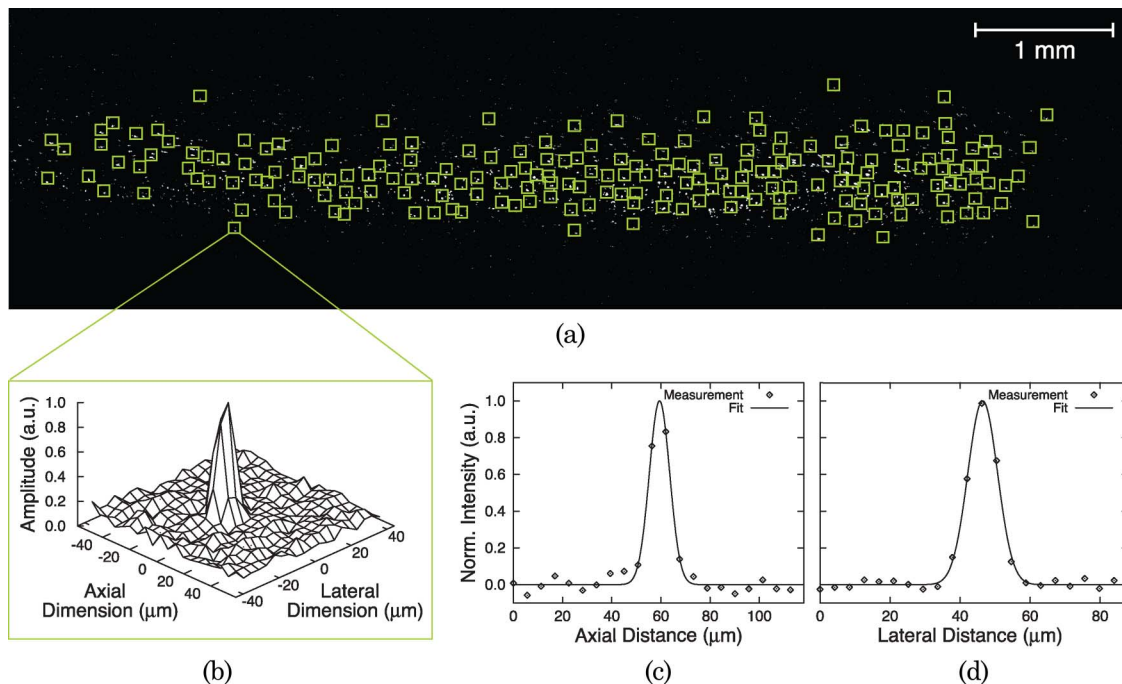


Fig. 3. (Color online) (a) Points identified from a single B-scan OCT image of a PSF phantom. (b) Surface plot of a single point with (c) axial and (d) lateral cross sections of a 2D elliptical Gaussian.

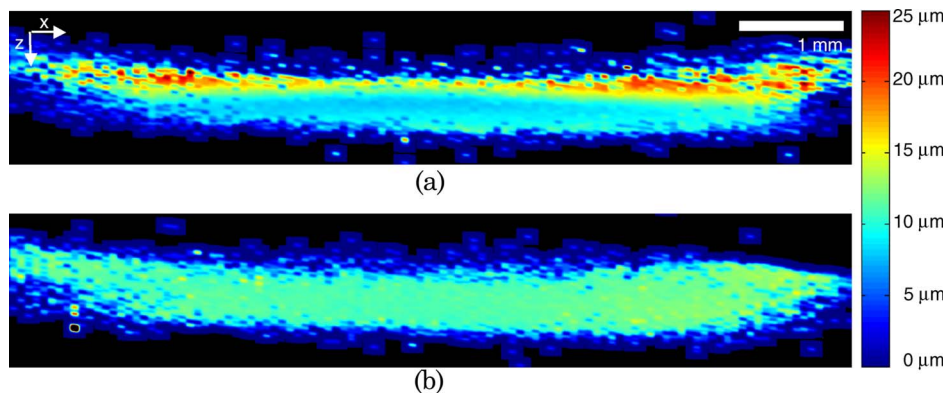


Fig. 4. (Color online) Spatial distribution throughout the B-scan image plane prior to deconvolution of (a) the lateral resolution and (b) the axial resolution.

The spatial distribution of Δx and Δz is represented by color maps in Figs. 4(a) and 4(b), respectively. The image space corresponds with the usual OCT B-scan image plane, while the color map indicates the respective measured resolution.

The axial cross section of Fig. 4, shown in Fig. 5 as diamond-shaped points, confirms the expected Gaussian beam waist predicted by Eq. (8) (solid curve). The circular points show a cross section at the same location, taken from the spatial map compiled after deconvolution of the spatial PSF.

Spatial maps for the lateral and axial resolution parameter after deconvolution are shown in Figs. 6(a) and 6(b). As with Fig. 4, the images represent the B-scan image plane and the color map encodes the deconvolved system resolution at the each spatial location. Areas of no color represent regions in which no measurement from the phantom was obtained.

In order to demonstrate the deconvolution efficacy, zoomed regions of a typical PSF phantom B-scan are shown in Fig. 7 (a) before and (b) after deconvolution. Subimages Fig. 7(a)i–iii and Fig. 7(b)i–iii highlight areas where the beneficial effect of deconvolution

can be qualitatively observed by the improved separation of clusters of points.

Quantitative analysis of the spatial deconvolution process is depicted in Figs. 8(a)–8(d). The histograms show the statistical distribution of resolution parameters before [Fig. 8(a) and 8(b)] and after [Fig. 8(c) and 8(d)] deconvolution. Figures 8(a) and 8(c) represent the measured lateral resolution and Figs. 8(b) and 8(d) represent the axial resolution.

5. Discussion

The multichannel OCT instrument used in this study did not have uniform sensitivity across the measured single channel field of view. This is a consequence of both Fourier domain detection and finite depth of field, of which the latter dominated. This is evident in Fig. 3, where points identified by the threshold filter are axially confined to the region of best focus and, therefore, highest sensitivity. Laterally, imaging sensitivity is also observed to drop, with no particles being detected toward the edges of the image. This is attributed to the increase in optical aberration present at the edges of the instrument sampling optics. In the OCT image [Fig. 3(a)], there are particles visible that have not been detected. This can be attributed to the logarithmic intensity scale of OCT images that artificially places low signal-to-noise (SNR) points on a comparable scale with those with high SNR. However, low SNR points are automatically rejected by the threshold filter. It is assumed that the majority of low SNR points are due to out-of-plane particles. Therefore, threshold rejection of low SNR points reduces multiple contributions from the same particle. Additionally, it is known from Mie theory that small variations in the particle diameter can substantially alter the backscattering coefficient and, hence, their detected intensity. Such points with low SNR are also rejected, but this is justified on the grounds that they occupy an insufficient number of image pixels to determine the system of equations required for a Gaussian fit. Approximation of the PSF by a 2D Gaussian function requires that there are a minimum of six data points within the measured PSF peak to obtain a fully determined fit. The localization of such data points is

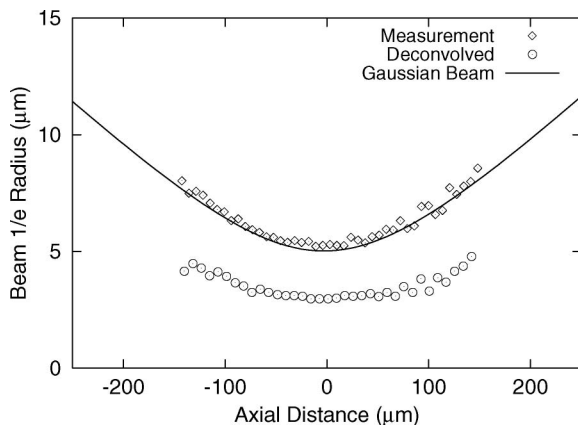


Fig. 5. Measured beam waist (diamond points) and simulated detected Gaussian beam waist using Eq. (8), where $w_0 = 7.1 \mu\text{m}$ and $\lambda_0 = 1310 \text{ nm}$. The beam waist after deconvolution is represented by circular points.

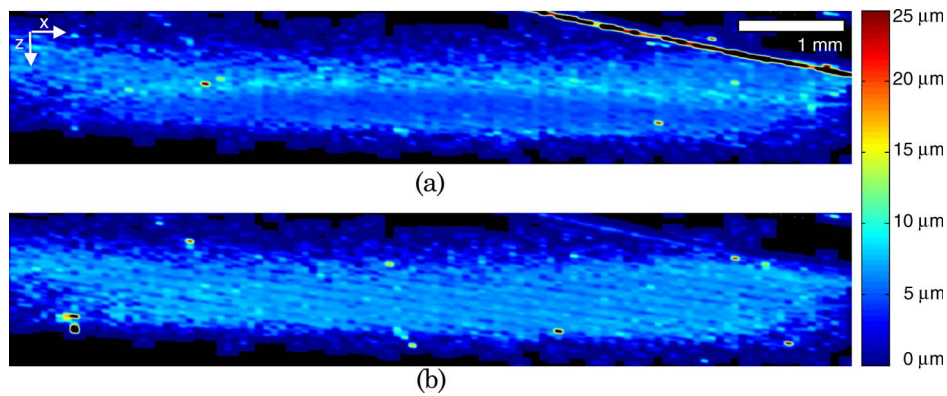


Fig. 6. (Color online) Spatial distribution throughout the B-scan image plane after deconvolution of (a) the lateral resolution and (b) the axial resolution.

an important factor for the fit quality. For example, low intensity data points away from the main peak do not adequately characterize the Gaussian function. Therefore, it is important that points used to estimate the peak parameters are well above the noise floor of the instrument. A 40% intensity threshold ensures that this criteria is met. Furthermore, Fourier domain detection over twice the source FWHM bandwidth limits axial pixel spacing to $\lambda_0^2/(4\Delta\lambda)$ and guarantees at least three axial data points define any peak above the 40% intensity threshold. The Michelson instrument has similar axial and lateral resolution with corresponding pixel spacings; therefore, the same expectation holds in the lateral dimension. Axial and lateral cross sections of an example PSF are shown in Figs. 3(c) and 3(d), respectively. These indicate that there are a sufficient number of measured points to obtain a successful fit, i.e., the system of equations is fully determined. This is important because while lateral sampling frequency can be addressed experimentally, sampling of the axial PSF in a Fourier domain OCT system is fundamentally limited by source and measurement bandwidth. One potential solution is to apply sinc interpolation by way of zero-padding the spectrum [23]; however, we found this to have a negligible effect on the results. The 2D resolution maps in Fig. 4 show a number of important features. They clearly demarcate the image field limits, although thus far we have been unable to quantify the instrument sensitivity associated with this boundary. However, revealed in the maps is a significant degree of spatial variation in both the lateral and the axial resolution. In depth, the lateral resolution variation was observed to follow the expected profile for a Gaussian beam, as shown in Fig. 5. However, toward the edges of Fig. 4(a), there is a pronounced degradation of the lateral resolution minima. Additionally, the waist minimum follows an arc across the image width. Within the arc it is clear that the lateral resolution is pushed to greater depths away from the image center. This can be explained as an effective reduction of the NA due to optical aberration as the sample beam scans away from

the middle of the focusing lens. A lower NA beam converges less rapidly to focus than one with a higher NA. Hence, gradual degradation of the NA over the lens diameter will lead to the observed arc in the measured waist. Furthermore, this is consistent with the observed decrease in lateral resolution as a function of lateral position. The axial resolution is expected to yield a spatially uniform distribution. However, as can be seen from Fig. 4(b), there is notable resolution loss outside of the middle third of the image width. Again, this may be attributable to lens aberrations away from the center of the imaging field. When the OCT probe beam passes through the focusing lens off center, the asymmetric optical path results in broadening of the axial PSF and a consequent loss of resolution. It is, therefore, encouraging that in Figs. 6(a) and 6(b), deconvolution of the spatially mapped PSF appears to have removed much of the transverse nonuniformity in both the

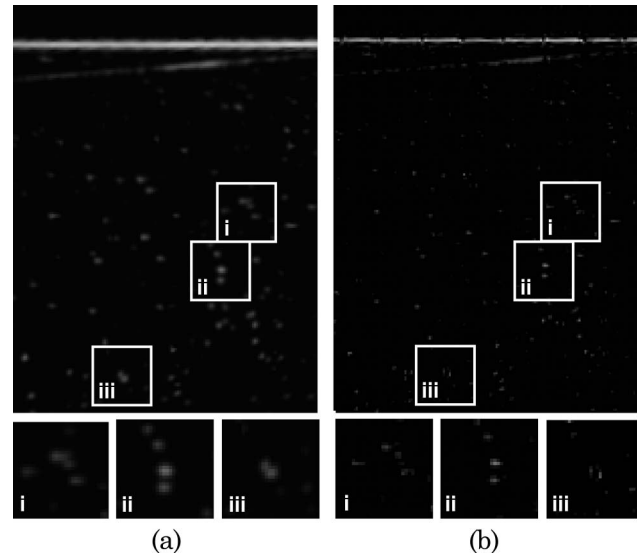


Fig. 7. Typical B-scan OCT images of the phantom (a) before and (b) after deconvolution. Three corresponding scattering point clusters are identified in each image by a surrounding white square. These subimages are enlarged below the main OCT images and labeled i, ii, and iii.

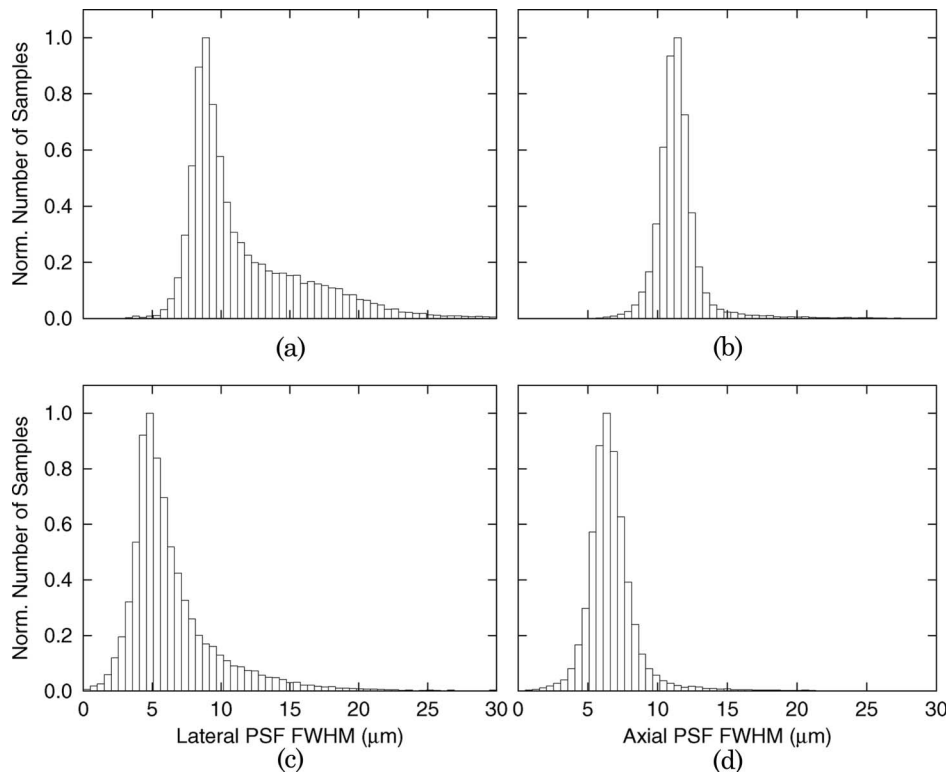


Fig. 8. Histograms of (a) lateral resolution prior to deconvolution, (b) axial resolution prior to deconvolution, (c) lateral resolution after deconvolution, and (d) axial resolution after deconvolution.

lateral and the axial resolution. There is, however, some residual lateral resolution loss toward the top and bottom of the depth of field, relative to the best correction. This is seen in both Fig. 6(a) and Fig. 5. However, over the central $100\text{ }\mu\text{m}$ depth of the beam waist, deconvolution has achieved an almost uniform resolution profile. The relative degree of correction at the top and bottom of the focal region is greater than in the center, yielding a net improvement over a purely Gaussian beam waist. The narrowing of the PSF on imaging performance is demonstrated in Figs. 7(a) and 7(b), where not only does the deconvolved image appear to be sharper, but the clusters of points marked as Figs. 7(a)i–iii and 7(b)i–iii show a clearly improved separation, indicative of a real resolution improvement rather than simply an image enhancement. Notable is Fig. 7(a)iii, in which the central signal cannot be clearly resolved into more than a single point, although there is some indication from the intensity pattern that at least two points are present. The deconvolution in Fig. 7(b)iii has clearly resolved the single point into two well-separated particles. The repeatability of this across similar points [i.e., Figs. 7(a)i–ii] strengthens the qualitative conclusion of resolution improvement. Quantitatively, the resolution enhancement is represented by the histograms in Fig. 8. The lateral resolution presents with an asymmetric distribution, Fig. 8(a), having a modal resolution of $\Delta x = 8.2\text{ }\mu\text{m}$. The tail, extending to higher resolution values, is dominated by contributions away from best focus. Far from focus there is insufficient sensitivity

to detect large numbers of particles within the phantom compared to within the focal region. A secondary contribution to the asymmetry of Fig. 8(a) is resolution variations due to lens aberrations. Aberrations due to the phantom itself are considered to be negligible. The high-quality optical finish applied to the phantom surface minimizes aberration. Spherical aberration induced by focusing through a refractive index discontinuity is also negligible for the low NA optics of the OCT system. Following deconvolution, Fig. 8(c) exhibits some recovery in the symmetry of the distribution, with notable reduction in the contribution of low resolution points. The spatial map shown in Fig. 6(a) confirms the resolution improvement across the field of view. From Fig. 8(c), the modal resolution is $\Delta x = 5.1\text{ }\mu\text{m}$, an improvement of $3.1\text{ }\mu\text{m}$. Figure 8(b) shows that the axial resolution yields a symmetric Gaussian distribution with a modal resolution of $\Delta z = 10.9\text{ }\mu\text{m}$. Following deconvolution the distribution, Fig. 8(d), maintains its shape but is shifted to the left with a mode of $\Delta z = 6.4\text{ }\mu\text{m}$ and improvement of $4.5\text{ }\mu\text{m}$.

6. Conclusions

This study has introduced the concept of a PSF phantom and demonstrated its application to the deconvolution of OCT images. The phantom enabled PSF measurement of a commercial OCT microscope at multiple spatial locations. By defining the resolution as the FWHM of the PSF, spatial resolution maps were formed that demonstrate significant nonuniformity in the OCT resolution in both lateral

and axial dimensions. An important contribution to this nonuniformity was optical aberration present in the system optics when scanned over a wide (8 mm) field of view. Therefore, these measurements are useful for optimizing the alignment and image width for OCT instruments.

Furthermore, we have demonstrated the advantage of spatially mapped PSF measurements for the purpose of deconvolution. Knowledge of PSF spatial variation enables deconvolution of a representative 2D PSF from corresponding locations within the image. This approach has worked well here, with deconvolution of the PSF phantom images revealing both qualitative and quantitative resolution improvement. Here, a 2D Gaussian function has been used to approximate the measured PSF. For the instrument evaluated, a Gaussian function was shown to be valid. However, this may not be generally true, especially where highly structured light sources are employed, or the incident beam is not Gaussian.

Having demonstrated this work using phantoms, it would clearly be advantageous to apply this approach to real tissue images. However, this would require a reasonable estimate of the relative refractive index difference between tissue and the phantom. In this study we have used the Lucy–Richardson deconvolution algorithm, with encouraging results. However, future studies should consider the relative advantages of different algorithms. The method presented here gives a useful quantitative way of performing such comparisons.

We gratefully acknowledge the financial support of the National Measurement Office. Reproduced with the permission of the Controller of Her Majesty's Stationery Office and the Office of the Queen's printer for Scotland.

References

1. C. M. C. Tempany and B. J. McNeil, "Advances in biomedical imaging," *J. Am. Med. Assn.* **285**, 562–567 (2001).
2. A. D. Robinson and R. K. Leach, "Overview of tomography techniques to measure wafer thickness in mems structures," NPL Report ENG 8 (National Physical Laboratory, 2008).
3. P. H. Tomlins and R. K. Wang, "Theory, developments and applications of optical coherence tomography," *J. Phys. D* **38**, 2519–2535 (2005).
4. W. Drexler, "Ultrahigh-resolution optical coherence tomography," *J. Biomed. Opt.* **9**, 47–71 (2004).
5. A. Dubois, G. Moneron, K. Grieve, and A. C. Boccara, "Three-dimensional cellular-level imaging using full-field optical coherence tomography," *Phys. Med. Biol.* **49**, 1227–1234 (2004).
6. R. K. Wang, V. V. Tuchin, X. Xu, and J. B. Elder, "Concurrent enhancement of imaging depth and contrast for optical coherence tomography by hyperosmotic agents," *J. Opt. Soc. Am. B* **18**, 948–953 (2001).
7. R. K. Wang, "Signal degradation by multiple scattering in optical coherence tomography of dense tissue: a Monte Carlo study," *Phys. Med. Biol.* **47**, 2281–2299 (2002).
8. B. R. Biedermann, W. Wieser, C. M. Eigenwillig, and R. Huber, "Recent developments in Fourier domain mode locked lasers for optical coherence tomography: imaging at 1310 nm vs. 1550 nm wavelength," *J. Biophoton.* **2**, 357–363 (2009).
9. T. S. Ralston, D. L. Marks, P. S. Carney, and S. A. Boppart, "Inverse scattering for optical coherence tomography," *J. Opt. Soc. Am. A* **23**, 1027–1037 (2006).
10. T. S. Ralston, D. L. Marks, P. S. Carney, and S. A. Boppart, "Interferometric synthetic aperture microscopy," *Nature Phys.* **3**, 129–134 (2007).
11. R. K. Wang, "Resolution improved optical coherence-gated tomography for imaging through biological tissues," *J. Mod. Opt.* **46**, 1905–1912 (1999).
12. J. M. Schmitt, "Restoration of optical coherence images of living tissue using the clean algorithm," *J. Biomed. Opt.* **3**, 66–75 (1998).
13. Y. Liu, Y. Liang, G. Mu, and X. Zhu, "Deconvolution methods for image deblurring in optical coherence tomography," *J. Opt. Soc. Am. A* **26**, 72–77 (2009).
14. A. F. Fercher, W. Drexler, C. K. Hitzenberger, and T. Lasser, "Optical coherence tomography—principles and applications," *Rep. Prog. Phys.* **66**, 239–303 (2003).
15. C. Akcay, P. Parrein, and J. P. Rolland, "Estimation of longitudinal resolution in optical coherence imaging," *Appl. Opt.* **41**, 5256–5262 (2002).
16. A. C. Akcay, J. P. Rolland, and J. M. Eichenholz, "Spectral shaping to improve the point spread function in optical coherence tomography," *Opt. Lett.* **28**, 1921–1923 (2003).
17. A. Yariv, *Optical Electronics*, 3rd ed. (Holt, Rinehart and Winston, 1985).
18. P. H. Tomlins, "Point spread function phantoms for optical coherence tomography," NPL Report OP2 (National Physical Laboratory, 2009).
19. M. Born and E. Wolf, *Principles of Optics*, 6th ed. (Pergamon, 1980).
20. J. D. Gaskill, *Linear Systems, Fourier Transforms, and Optics* (Wiley, 1978).
21. J. Holmes, S. Hattersley, N. Stone, F. Bazant-Hegemark, and H. Barr, "Multi-channel fourier domain OCT system with superior lateral resolution for biomedical applications," *Proc. SPIE* **6847**, 684700 (2008).
22. R. C. Gonzalez and R. E. Woods, *Digital Image Processing*, 3rd ed. (Prentice Hall, 2008).
23. C. Dorrer, N. Belabas, J.-P. Likforman, and M. Joffre, "Spectral resolution and sampling issues in Fourier-transform spectral interferometry," *J. Opt. Soc. Am. B* **17**, 1795–1802 (2000).